Statistical point cloud model to investigate measurement uncertainty in coordinate metrology

N. Senin[1,2]*, S. Catalucci[1], M. Moretti[2] and R.K. Leach[1]

[1]Manufacturing Metrology Team, Faculty of Engineering, University of Nottingham, UK
[2]Department of Engineering, University of Perugia, Perugia, Italy
*nicola.senin@nottingham.ac.uk

Abstract

In this work an approach to investigate measurement uncertainty in coordinate metrology is presented, based on fitting Gaussian random fields to high-density point clouds produced by measurement repeats. The fitted field delivers a depiction of the spatial distribution of random measurement error over a part geometry, and can incorporate local bias information through further measurement or with the use of an external model to obtain a complete, spatial uncertainty map. The statistical model also allows the application of Monte Carlo simulation to investigate how error propagates through the data processing pipeline ultimately affecting the determination of features of size and the verification of conformance to specifications. The proposed approach is validated through application to simulated test cases involving known measurement error, and then applied to a real part, measured with optical and contact technologies. The results indicate the usefulness of the approach to estimate measurement uncertainty and to investigate performance and behaviour of measurement solutions applied to the inspection and verification of industrial parts. The approach paves the way for the implementation of automated measurement systems capable of self-assessment of measurement performance.

1. Introduction

Despite optical coordinate measuring systems (CMSs) being commercially available for at least two decades, there is still not a complete framework for their calibration and verification. The optics manufacturing industries have well-established calibration infrastructures for optical measurements of surface form, albeit for very specific surface types [1]. However, these infrastructures are less developed for many precision manufacturing industries that rely on machining of complex surface geometries [2,3]. Highly complex freeform geometries, as found for example in the automotive, aerospace and medical parts industries, mean that many of the established calibration techniques for optical surface measurements may not be directly relevant. In addition, with the industrial uptake of additive manufacturing techniques, the complexity of the resulting geometries is leading to new measurement challenges [4,5].

When manufacturing complex surfaces, industrial instrument users rely on well-established techniques to demonstrate that a process is under control and that the response of an instrument is not changing significantly with time. Examples found in common practice include statistical process control [6], gauge R&R studies [7] and measurement system analysis [8]. Whilst these approaches are mature and clearly allow manufacturing to continue and advance, they do not lead to a culture of uncertainty estimation in manufacturing and, hence, tolerancing of complex surfaces is difficult and geometrical product specification principles cannot always be applied.

Looking from a different perspective, it is commonplace in many manufacturing industries to hear users expressing alarm about the incompatibility of optical instruments with contact methods for coordinate metrology, and these concerns are often borne out in comparisons (for example, [9–11]). In many cases, the difference between the results from optical and contact instruments can be explained after critical assessment of the measurement conditions and sample geometries [12]), but there is still an undercurrent of concern in some industries.

It is a difficult task to estimate the uncertainty for a CMS measurement from first principles, even for measurement of a simple prismatic component, for example a smooth sphere. The large number of influence factors and complex nature of CMS probing strategies mean that, in many cases, an analytical

expression for the measurement model cannot easily be found. For this reason, ISO Technical Committee 213 working group 10 have developed a number of strategies for uncertainty estimation, at least for contact CMS [13]. Strategies for non-contact CMSs remain an open research area, although there has been some recent work highlighting the issues [5,14–17].

As with measurement uncertainty, traceability of measurements carried out by CMSs is difficult to demonstrate. It used to be the case that the only way to demonstrate traceability was to carry out ISO 10360-type performance verification tests on the CMS. However, if a CMS is performance-verified, this does not automatically mean that measurements carried out with this CMS are calibrated and/or traceable. A performance verification only demonstrates that the machine meets its specification for measuring simple lengths, i.e. it is not task specific. ISO Technical Committee 213 Working Group 10 is still developing a part that addresses the performance verification of optical CMS (ISO 10360 part 13 (2020) [18]). Due to the current lack of a published ISO standards in this area, the German VDI/VDE 2634 part 3 (2011) [19] guideline is often used in practice for performance verification of optical CMS.

A better method to achieve at least a degree of traceability is described in ISO 15530 part 3 (2011) [20]. This specification standard makes use of calibrated artefacts to essentially use the CMS as a comparator. The uncertainty evaluation is based on a sequence of measurements on a calibrated object or objects, performed in the same way and under the same conditions as the actual measurements (this is known as the "substitution method"). The differences between the results obtained from the measurement of the objects and the known calibration values of these calibrated objects are used to estimate the uncertainty of the measurements. As an example, if an external dimension needs to be measured, a calibrated length bar of similar length can be mounted adjacent to the object being measured, and the measurement carried out as a comparison while assuming certain similarity conditions are applied (for example, similar materials, thermal expansion coefficients, surface conditions and measurement conditions). This ensures that many of the systematic influence factors are common to both measurements and, therefore, reduced combined uncertainty. Uncertainty estimations for CMSs using the substitution method are not usually performed on complex parts due the difficulty and expense of developing a calibrated artefact to compare with the workpiece.

Alternative methods can be used to determine the task-specific uncertainty of coordinate measurements. One such method, that evaluates the uncertainty by Monte Carlo methods, is described in ISO/TS 15530 part 4 (2008) [21]. To allow CMS users to easily create uncertainty statements, CMS suppliers and other third-party companies have developed uncertainty-evaluating software, also known as "virtual CMMs" [22,23], but such software is only available for contact probes. Determination of measurement uncertainty using a virtual CMS is carried out by performing repeated simulated measurements with varying inputs (influence quantities) on a simulated CMS and determining how those inputs affect the measurand. The software determines the variability that will occur with the physical CMS measurements with a modelling of the uncertainty contributions for each point measured by the CMS. Known systematic uncertainty contributions remain determined by their influencing factors, e.g. temperature, while unknown systematic and random contributions are varied in each simulated measurement throughout their ranges. This simulation is repeated a significant number of times until a statistical evaluation of these virtual measurements is made, and the expanded uncertainty is reported.

It is relatively simple to understand and model the physical interaction of a contact probe tip with a surface, but it not so simple to model the equivalent optical interaction, and this is a significant part of the uncertainty problem [24]. There has been some recent activity on modelling optical systems with virtual instruments in mind [16,17,25], but there is still a lot to do and the issues are not yet under development in ISO Technical Committee 213 Working Group 10.

Most current technologies for the inspection and verification of form are centred around the measurement and manipulation of point cloud surface data. Tactile CMSs sample surfaces at specific locations using contact probes, optical CMSs are typically capable of high-density point-based sampling of surfaces within line-of-sight [26]. X-ray computed tomography performs volumetric sampling of density, but surfaces can be extracted via thresholding and often sampled into point-based representations [27]. When dealing with measurement uncertainty, the central role of point cloud surface data is often overlooked. However, clearly each digital point is the result of a chain of events and physical phenomena that define the measurement process and which result in some form of associated positional uncertainty (i.e. uncertainty on where the point should be actually located in absence of measurement error). Analogously, any dimensional or geometric assessment deriving from point cloud analysis and manipulation should be associated to an uncertainty that comes from the propagation of point positional uncertainty and additional error sources introduced by the processing methods and algorithms. A proper reconstruction of the chain of events that lead to the propagation of point positional uncertainty into a final

inspection/verification result, for example the assessment of a dimension, or a tolerance interval, would play a relevant role towards a better understanding of measurement error in industrial metrology.

Point positional uncertainty has been addressed by multiple authors in different scientific contexts. For example, Pauly et al. [28] consider the problem of surface reconstruction from a point cloud, assuming the point cloud as a finite set of noisy samples that provide incomplete information about the underlying surface. To capture uncertainty about the surface, they introduce a statistical representation that quantifies for each point in space the likelihood that a surface fitting the data passes through that point. This likelihood map is constructed by aggregating local linear extrapolators computed from weighted least-squares fits. The quality of fit of these extrapolators is combined into a corresponding confidence map that quantifies the quality of local tangent estimates. The relationship between measurement uncertainty and fitting has been investigated also by Forbes et al. [29–31] as a means to determine the uncertainty in the characterisation of form error. The variability in point clouds has been investigated in relation to discrete, point-based skin models in the field of geometric tolerancing [32–34]. A skin model is a surface model capable of representing geometric variability across manufactured instances of the same part. Both deviations of point placement in three-dimensions have been investigated [32] and deviations defined in the direction of the local surface normal [33], combined with the use of Markov chains Monte Carlo, Gaussian random fields (GRFs) and other methods from statistical shape analysis [34].

Univariate random variables associated with local surface normals have also been explored [35], in this case specifically as a means to address measurement uncertainty in surface topography measurement, and not variability across surface instances. Random variables may be defined as independent between points. Alternatively, spatial dependency can be captured by modelling co-variance, as carried out for discrete skin models [32]. Statistical point cloud models dedicated to addressing measurement uncertainty can be built by aggregating repeat measurements, or by fitting an individual measurement (single point cloud), as long as specific assumptions are made. For example, Evans [36] has demonstrated how standard deviation maps computed from repeated height observations can be propagated into the assessment of peak-to-valley form error for a flat surface, using Monte Carlo simulation. Standard deviation maps obtained from measurement repeats are also useful for calibration and more general tasks related to uncertainty assessment [1,37]. A statistical model from measurement repeats has also been obtained from a focus variation measurement of surface topography, by fitting the measured point cloud to a Gaussian field using a shift-invariant model for covariance defined using a covariogram [38]. The use of spatial statistics based on Gaussian fields, in particular kriging, has been investigated [39], where a method to directly derive form error from the kriging model was presented, and the relationships with point-based sampling investigated. More recently, kriging models have been used to estimate uncertainty and calibrate non-contact CMSs [40].

Several other approaches have been presented in the literature revolving around representing point location error as a 3D ellipsoid. For example, Ozendi et al. [41] propose a model to determine the error ellipsoid of single points in terrestrial laser triangulation as a means to assess measurement precision. Terrestrial laser triangulation is also addressed by Chen et al. [42], where point positioning error is again represented as a 3D ellipsoid, assuming a Gaussian distribution and using covariance to capture dependencies amongst points. Overlapping ellipsoids belonging to neighbouring points could be merged into a single volume representing the random error of the entire cloud (i.e. precision). Single point error ellipsoids are also used by Du et al. [43,44] to model measurement uncertainty in laser radar measurement systems. Once the ellipsoid has been estimated for each point, error propagation through datum fitting processes can be investigated.

This work is organised as follows:

- in the materials and methods section, first we present a method to aggregate measurement repeats (point clouds) in order to build a statistical model representing the random component of positional uncertainty of the measured points. The statistical model is comprised of a Gaussian random field (GRF) and a vector field that maps the GRF to any three-dimensional geometry;
- we show that the statistical model can be used to obtain spatial maps of random error associated with the points of any point cloud, and can also be used to estimate the random error component associated with linear dimensions computed, starting from the point cloud;
- we illustrate how a separately sourced spatial map of bias can be combined with the statistical model, in order to achieve a more comprehensive map of positional uncertainty associated with a point cloud. Two possible ways to obtain a bias map are discussed: through a separate set of more accurate measurements of the same part, or through the use of a mathematical model capable of predicting local bias, assuming such a model is available;

- we introduce a validation method that is exclusively dedicated to assessing accuracy and precision of the proposed method in the estimation of the random component associated to linear dimensions. The validation method fully relies on simulation so that estimates can be compared against known references and performance can be assessed in a quantitative way. This validation method does not address bias;
- in the results section, first we illustrate results of the validation method applied to two simulated test cases. We replicate a scenario where a few measurement repeats are available from a test part, and we compare the random error component on linear dimensions as assessed by using solely the repeats, against using the statistical model fitted to the same repeats. We show that the use of the statistical model leads to improved accuracy and precision in the estimation of the random error compoment associated with linear dimensions. As stated earlier, this validation does not address bias;
- through the use of a real test case (optical and contact measurement of a real part) we demonstrate the use of the statistical model in a scenario where a separate estimate for bias can be constructed from a set of more accurate measurement repeats, and aggregated to the random error component estimated by our statistical model. The use of such an approach is discussed in research laboratory scenarios where the goal is to investigate performance and behaviour of coordinate measuring systems.

The main challenges and open issues in relation to the proposed approach are illustrated in the discussion, and a summary of our findings is reported in the conclusions, in particular addressing what role the proposed method can have in the broader problem of investigating measurement uncertainty.

2. Materials and methods

In this work, we consider high-density point clouds existing in a 3D Cartesian space and obtained by measurement. We address the mathematical representation of positional uncertainty of each point in the point cloud, where positional uncertainty is referred to a lack of knowledge of where each point of the cloud is located in space, with respect to where it should be assuming an ideal measurement (i.e. with an absence of measurement error). In the following, lack of knowledge of point position is assumed as solely caused by the measurement error. However, our model could be adapted to handle uncertainty in where the measured surface is located, which would be due to manufacturing error.

2.1. One-dimensional model of point positional uncertainty

Whilst positional uncertainty may be defined in 3D around each point [41,43,44] (Figure 1.a), in our approach, we consider the positional uncertainty of each point as a scalar quantity measured along a specific directional vector, normal to the local orientation of the surface from which the point has been measured (Figure 1.b), similar to that reported elsewhere [33,35].
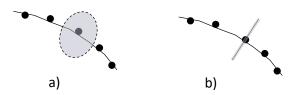

Figure 1. Models of positional uncertainty for points belonging to a measured point cloud. A) 3D model (uncertainty on the position of a point is defined in vector form, with components along all three Cartesian axes; b) one-dimensional model: uncertainty modelled as a scalar value, directed along the surface local normal.

The choice of modelling positional uncertainty as a scalar value directed along the local normal is driven by the observation that in planar datum fitting, point displacements orthogonal to the plane influence the fitting result more than displacements on the plane. This consideration specifically applies to high-density sampling. On the contrary, if the point cloud was low-density, for example as measured by a conventional contact CMS, then fewer points would be used to fit each geometric entity, and the position of individual points, as measured in all directions, would typically be more relevant for dimensional and geometric inspection and verification.

In this work, under the assumption that the relevant positional deviation of each point is the one measured orthogonally to the local surface fitted through that point, positional uncertainty can be expressed as a

unidimensional interval, and the distance of each real point with respect to its ideal counterpart (i.e. that obtained with no measurement error) can be expressed by a scalar value.

2.2. Using a discrete, Gaussian random field (GRF) to represent positional uncertainty

The distance of each measured point to its ideal positional counterpart (a scalar value) can be modelled by a unidimensional random variable. Given a point cloud comprised of N points, N random variables are needed, forming a finite and countable set. As these random variables are associated to points in space with finite spacing from each other, they can be modelled as a (discrete) random field. In our formulation (Figure 2), each random variable Z_i in the random field (where i is the index of the point in the cloud) is associated with an origin point o_i and to a directional vector (represented by the local surface normal n_i) that defines a local coordinate system (z_{loc}). The purpose of o_i and n_i is to map the scalar value of the random variable into a one-dimensional interval aligned to the direction along which the positional uncertainty of each point is supposed to be captured.

The origin point o_i acts as the location of the random variable in the 3D Cartesian space, and is also needed to set a reference zero ($z_{loc} = 0$) in the local coordinate system. Note that the position of the origin point o_i along the local normal is not necessarily meant to represent the result of an ideal measurement (i.e. a measurement with no error), a concept which will be discussed later in this section.
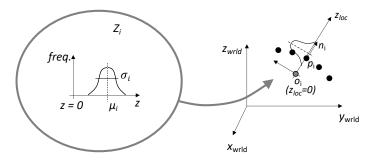

Figure 2. The ith variable Z_i of the random field is associated to the point p_i of the cloud. The random scalar value is mapped to the three-dimensional point cloud space through an origin point o_i (location) and an orientation vector defined by the local normal n_i.

The discrete random field considered in this work is assumed Gaussian. In a GRF, each random variable is defined by a normal distribution (and hence is fully defined by its first and second order moments – mean and variance), and each subset of M random variables extracted from the field of N variables is also defined by a normal, multivariate (i.e. M-dimensional) joint probability distribution.

A Gaussian discrete random field of N variables $\{Z_1, Z_2, \cdots, Z_N\}$ is fully defined by a vector of mean values μ (i.e. first order moments) and a matrix K of covariance values (i.e. second order moments) covering all the pairwise associations between variables belonging to the field, that is:

$$\mu = \{\mu_1, \mu_2, \cdots, \mu_N\}, \qquad K = \begin{bmatrix} k_{1,1} & \cdots & k_{1,N} \\ \vdots & \ddots & \vdots \\ k_{N,1} & \cdots & k_{N,N} \end{bmatrix} \tag{1}$$

where μ_1 is the mean of Z_i, $k_{i,j}$ is the covariance of the pair Z_i, Z_j and $k_{i,i}$ is the variance of Z_i. The random field $Z(\mu, K)$ can be associated to a point cloud of N points: $\{p_1, p_2, \cdots, p_N\}$ and local normals $\{n_1, n_2, \cdots, n_N\}$ through a series of origin points $\{o_1, o_2, \cdots, o_N\}$ to set the zeros of the random variables.

Using the above formal representation, local positional uncertainty is described as a scalar quantity, but mapped to a vector field that defines its position and orientation in space. In other words, the local normals $\{n_1, n_2, \cdots, n_N\}$ and the origin points $\{o_1, o_2, \cdots, o_N\}$ establish a spatial mapping between the scalar random field, representing local height (Z) as random variables over a flat space, and a full 3D surface defined by a series of points and their local normals. Notably, the set $\{o_i, n_i\} \, \forall i \in \{1, \cdots, N\}$ is, therefore, the vector field which allows mapping of a GRF of scalar quantities into the fully three-dimensional space of the part.

Local orientation in space does not influence the definition of the random field, so long as the first and second order moments for the random variables are fully defined. It is important to point out that the same formulation can be adopted for very different geometric datasets, ranging from height/elevation maps (all heights defined along a single direction - Figure 3.a) to full 3D point clouds or vertex meshes (Figure 3.b) where local heights are arbitrarily oriented in space.
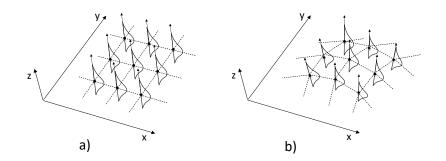

Figure 3. The proposed formulation of discrete random field and its spatial mapping to three-dimensional Cartesian space allows for adopting the same formulation for a) height maps and b) fully three-dimensional point clouds.

2.3. Challenges of fitting the random field

For a fully defined GRF containing N random variables, N first order moments (mean values, i.e. the vector $\mathbf{\mu}$) and $N \times N$ second order moments (covariance values, i.e. the matrix $\mathbf{K}$) must be known (however, consider that $\mathbf{K}$ is symmetric, so $k_{i,j} = k_{j,i}$). If only one point cloud is available, we only have one observation (point) for each random variable. Since such observational data is insufficient to fully determine the mean vector $\mathbf{\mu}$ and covariance matrix $\mathbf{K}$, some assumptions must be made on the nature of mean and covariance to simplify the problem. Typical assumptions, in particular from the literature on Gaussian processes [45,46], resort to the concept of shift-invariance, i.e. the mean and variance are considered independent of position in space, and covariance is considered only dependent on the relative distance between the random variables [45]. Shift-invariance implies constant mean and variance, and covariance defined using kernel functions that are only dependent on the relative distance between each pair of variables, for example the squared exponential or a Matérn kernel [47]. The assumption of shift-invariance reduces the unknowns in the fitting problem, which can be solved, for example, via maximum likelihood estimation [45]. However, shift-invariance typically implies that the local properties of the field are the same everywhere (in particular, all the random variables have the same mean and same variance); this is clearly contrasting with previous experimental observations obtained by performing repeat measurements of the same surface [35,48] that, for example, showed that the local scatter of height values (related to local variance) depends on local geometric properties of the measured surface, i.e. they are not shift-invariant.

Another option adopted for fitting the random field is to consider all the random variables of the field as independent, which removes the need to solve the full covariance matrix, and reduces the fitting problem to a determination of the mean vector $\mathbf{\mu}$ and the variance terms $k_{i,i}$ in the principal diagonal of the covariance matrix $\mathbf{K}$ (other covariance terms being zero). This means that each random variable can be estimated separately, starting from its first and second order moments, by simply using the observations available at each location as, for example, in previous work [35].

2.4. Proposed approach for fitting the GRF

In this work, as opposed to assuming shift-invariance, we rely on having repeat measurements as a source of additional information to solve the fitting problem. The overarching idea is that multiple point clouds obtained from the same surface result in multiple observations for any given location (Figure 3.a), i.e. more observations to attempt a direct estimation of the vector of means from the available samples, and of the covariance matrix from sample covariance.

For practical purposes, despite the high density of points, neither the existence of multiple points in correspondence to the same normal nor the alignment of local normals from different clouds can be expected (Figure 3.b). Hence, to achieve a result similar to that shown in Figure 3.a, we propose the following procedure:

- we rely on the availability of a CAD model (for example, a triangle mesh) to drive the alignment of the point clouds;

- we use one of the point clouds as the reference to define the resampling locations (i.e. the locations at which the GRF is defined) and the local normal;

- we resample the other clouds at the intersections with the local normal to the reference point cloud, using linear interpolation on the other clouds (Figure 3.c); and

- the intersection of the local normal with the CAD surface defines the origin point to which the local z values of each random variable are referred.

Using this procedure, as many observations as the number of available measurement repeats are obtained for each random variable (Figure 3.d).
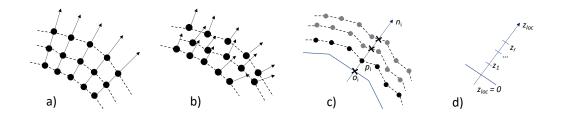

Figure 4. How the measurement repeats are used to create observations for each random variable Z_i (in the example, portions of three point clouds are shown, the points of each cloud rendered as connected by an imaginary, dotted line); a) ideal scenario: at any given location, observations from multiple clouds are natively available and all share the same local normal; b) real scenario: points from different repeats will not be aligned at shared locations, and each point may have a potentially different normal if computed using neighbours in the same cloud; c) proposed solution: the points of one cloud act as reference locations (e.g. $\boldsymbol{p}_i$); the local normal computed for $\boldsymbol{p}_i$ (e.g. $\boldsymbol{n}_i$) is used as reference direction; the other point clouds are resampled by interpolation at the intersections with the local normal; the intersection of the local normal with the CAD surface is assumed as the origin point $\boldsymbol{o}_i$; d) the computation produces multiple observations for the Z_i random variable in its local coordinate system z_{loc} (the entire process is repeated for each point of the reference point cloud).

Clearly, in the proposed procedure, a) the choice of one of the clouds as localisation and orientation reference introduces an element of arbitrariness, as any other cloud could be used, including any other reference set, for example, sampled directly from the CAD surfaces; b) using points from the CAD surface as origin points does indeed convert all the other points into distances from the nominal surface, but one should be careful not to mistake such distances as measurement error, as there is no information on how much the local, real surface deviates from the nominal one (more on this later in this section).

Regardless of the above considerations, after resampling is performed on R measurement repeats (point clouds), R observations $z_{i,r}$, $\forall r \in \{1, \cdots, R\}$ are available for each random variable Z_i. These observations are referred to a local origin point $\boldsymbol{o}_i$ ($z_{loc} = 0$) on the CAD surface, and act as a random sample to describe Z_i, and there are as many samples as the number N of random variables in the GRF.

In this situation, each sample mean:

$$\bar{z}_i = \frac{\sum_{r=1}^{R} z_{i,r}}{R} \tag{2}$$

can be used as an estimator of the corresponding population mean μ_i in the vector $\boldsymbol{\mu}$. However, let us consider the covariance matrix $\mathbf{S}$ of the sample, defined by the terms $s_{i,j}$ for the pair of random variables Z_i, Z_j, i.e.

$$s_{i,j} = \frac{\sum_{r=1}^{R}(z_{i,r}-\bar{z}_i)\cdot(z_{j,r}-\bar{z}_j)}{R}. \tag{3}$$

Unfortunately, the covariance matrix $\mathbf{S}$ of the sample is not a good estimator for the covariance matrix $\mathbf{K}$ of the GRF (i.e. each sample covariance term $s_{i,j}$ is not a good estimator of the population covariance term $k_{i,j}$) because the number of dimensions in the random variables (i.e. the number of points N in the field) is much larger than the number of observations R available for each point (i.e. the number of repeats). Several different approaches can be adopted to estimate $\mathbf{K}$. In this work, we use the oracle shrinkage approximating estimator of the covariance, as detailed elsewhere [49].

2.5. Using the statistical model to investigate the spatial distribution of random measurement error in relation to a specific test part

The first use of the statistical model is to investigate how random measurement error is spatially distributed on the different surfaces of a part. A simplified representation of the type of information that can be obtained is illustrated in Figure 5.

a)   b)
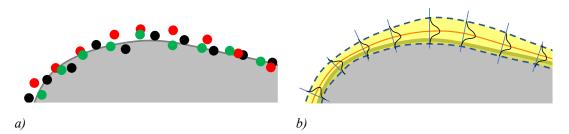
Figure 5. Schema of the type of information which can be obtained from the use of the proposed statistical modelling approach (simplified in two-dimensions); a) original measurement repeats (point clouds, each repeat is shown in a different colour) in relation to the associated CAD model of the part (gray); b) spatial map of the mean (red line) and variance (yellow band) of the statistical model fitted on the point clouds. The yellow band is an interpolation of local $\pm 3\sigma$ values computed on the marginal probability distributions of the local random variables of the GRF.

As shown in Figure 5, spatial maps can be obtained, representing the mean function and the variance as estimated by the statistical model. Variance describes local scatter of the measurement orthogonal to the underlying surface lay; the estimation takes into account any spatial dependency which may exist between neighbouring measured points because of how the GRF is defined. The mean function indicates central tendency of the measurement, i.e. the most frequent localisation of the point cloud with respect to any specific surface region on the underlying CAD model. The interpretation of central tendency is particularly critical, because any non-zero displacement of the mean function with respect to the underlying CAD surface may be due to either measurement bias, or the real part being different from the nominal model (manufacturing error) or, most commonly, due to both aspects. Further discrimination is not possible because the statistical model is based on measurement repeats and, therefore, it cannot capture any error component that is invariant across repeats.

An analysis such as that illustrated in Figure 5 may be useful in the routine inspection of manufactured parts in a production scenario, as long as the execution of measurement repeats is viable, and as long as the interest is to characterise random error components visible across repeats. We believe that such an analysis would probably be more useful in research laboratory scenarios where the goal is to perform a more detailed investigation of the metrological performance and behaviour of coordinate measuring systems/measurement technologies applied to specific types of geometries, materials, aspect ratios, etc.

2.6. Generating new point clouds from realisations of the random field

Another use of the proposed statistical modelling approach is to generate new "virtual" point clouds. Once the GRF has been fitted, a new realisation of the random field, also referred to as a new observation, is a new set of values for all the random variables in the field, i.e. $\{z_1, z_2, \ldots, z_N\}$. These scalar values can be mapped back into 3D space to generate a new point cloud. The new realisations of the random field can be obtained by applying the Cholesky decomposition on the covariance matrix $\mathbf{K}$. The Cholesky decomposition of $\mathbf{K}$ (assumed Hermitian, positive-definite) leads to a lower triangular matrix $\mathbf{L}$ so that:

$$\mathbf{K} = \mathbf{LL}^* \tag{4}$$

where $\mathbf{L}^*$ is the conjugate transpose of $\mathbf{L}$. Assuming $\mathbf{K}$ is symmetric (which is the case for the variance-covariance matrix), then $\mathbf{L}^*$ is simply $\mathbf{L}^\mathbf{T}$, and because $\mathbf{K}$ is real-valued, $\mathbf{L}$ is also real. Then, each scalar value $z_{i,new}$ representing a component of the new realisation of the field, can be obtained as:

$$z_{i,new} = \mu_i + N(0,1)\mathbf{L} \tag{5}$$

where μ_i is the ith entry in the vector of means $\boldsymbol{\mu}$ and $N(0,1)$ is a new observation drawn from a standard normal (zero mean and unit variance).

Once all of the $z_{i,new}$ values have been obtained, the new point cloud, constructed from points $\{\boldsymbol{p}_{1,new}, \boldsymbol{p}_{2,new}, \cdots, \boldsymbol{p}_{N,new}\}$, can be obtained by mapping each $z_{i,new}$ value back into the 3D space of the point cloud, i.e:

$$\boldsymbol{p}_{i,new} = \boldsymbol{o}_i + z_{i,new} \cdot \boldsymbol{n}_i \tag{6}$$

where $\boldsymbol{o}_i$ is the ith local origin point and $\boldsymbol{n}_i$ is the local normal, as previously defined in Section 2.2.

2.7. Assessing the uncertainty associated with results of a point cloud processing pipeline using Monte Carlo simulation

Once the GRF is fitted, an arbitrary number of new observations can be generated from it, to study error propagation in point cloud processing using Monte Carlo methods. The procedure is summarised in Figure 6. A typical point cloud processing pipeline for inspection and verification in coordinate metrology consists primarily of segmentation of the point cloud and fitting of different segments (subsets of neighbouring points) to datum surfaces. Geometric datums are then used to infer geometric properties related to distance, length, parallelism, concentricity, etc. [13]. In a Monte Carlo simulation, the same data processing pipeline can be applied to the new observations (point clouds) generated by the GRF (Figure 6), and any intermediate or final scalar result from the pipeline can be sampled from repeats into a probability distribution, which can later be assessed for central tendency and dispersion. The same approach may be identically applied to a final result of the characterisation (for example, an Euclidean distance between two surfaces), or to any intermediate result (for example, the direction cosines of a datum plane fitted to a specific segment of a point cloud).
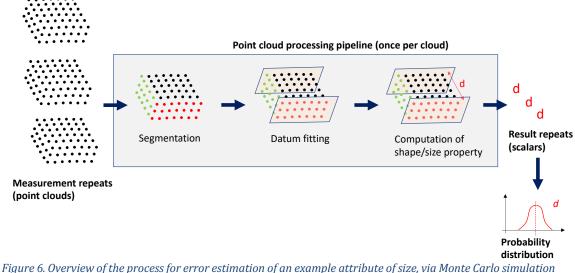
Figure 6. Overview of the process for error estimation of an example attribute of size, via Monte Carlo simulation and GRF (the GRF is used to generate the measurement repeats - point clouds).

When the goal is the characterisation of surface texture, the same approach can be applied, as there will be a dedicated pipeline consisting of form removal, band-pass filtering and computation of texture parameters. Again any scalar quantity that can be extracted from the pipeline could be subjected to statistical characterisation by running Monte Carlo simulations using new realisations generated by a fitted GRF.

Clearly, simple statistics of the selected characterisation results could also be obtained by applying the point cloud processing pipeline only to the available measurement repeats. However, the results would evidently suffer from the small sample sizes. Measurement is costly and resource intensive compared to obtaining point clouds by simulation; the purpose of the developed statistical model is to allow for the generation of new virtual point clouds that are more faithful to the original observations, in that they replicate their statistical properties.

2.8. Incorporating bias

A GRF fitted on a series of measurement repeats will provide information about local point scatter in the direction defined by the local reference normals. Central tendency, defined by the vector $\boldsymbol{\mu} = \{\mu_1, \mu_2, \cdots, \mu_N\}$, is expressed with reference to the vector of origin points $\mathbf{o} = \{o_1, o_2, \cdots, o_N\}$, typically computed from intersections with the CAD surface. Whilst the GRF captures dispersion of the points across measurement repeats, bias with respect to an ideal measurement (i.e. a measurement with no error) cannot be estimated because central tendency as captured by $\boldsymbol{\mu}$ is referred to the nominal model, and may not necessarily be representative of the real part that has been measured (for example, if the real part is warped with respect to the nominal geometry). To incorporate bias, the solution illustrated in this work proposes two alternative routes. The first route is that a mathematical model is assumed available, capable of producing a bias value and associated uncertainty interval, mapped to each location of the part surface. Such a model may be produced using one of the approaches proposed in the literature, as reviewed in Section 1.

The second route assumes that another set of measurement repeats can be taken using a measurement solution recognised as more accurate and with an associated measurement uncertainty. A typical scenario would consist of taking a second set of measurements with a traceable tactile CMS. Once the second set of repeats is available, a second GRF can be constructed using the same methods given in Section 2.4. Because the two GRFs have been built using the same CAD model as reference, spatial co-localisation can be achieved ensuring that all the point clouds from the repeats of both instruments have been registered to the same reference mesh. Once both the GRFs are available, to assess bias, the Euclidean distance between the mean vectors of the two models can be used. However, because in general the two GRFs will not have been sampled in the same positions (although being aligned), interpolation of one of the two mean functions is necessary to obtain bias (Figure 7). The same interpolation procedure

previously illustrated in Section 2.4 can be applied. Such an approach works better if the point clouds have similar densities, to reduce additional error potentially introduced by relying on interpolation.
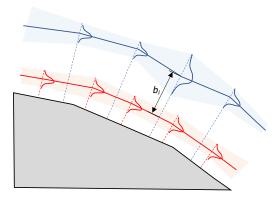

Figure 7. Procedure to assess bias between two GRFs. In the figure, the original GRF is represented in blue, the second GRF (more accurate reference) is in red. The distances have been amplified for clarity. Local bias is computed starting from the mean function defined from first GRF, using the locations of the random variables in the first GRF and the related normals. The intersections with the mean function of the second GRF are found and used to determine bias (bias for the ith point is shown in the figure). If the second GRF has an associated uncertainty $\pm U$, said uncertainty can be incorporated in the bias ($b_i \pm U$).

2.9. Validation and performance assessment

A validation method is proposed based on simulation, so that the performance of the proposed approach can be compared with known target results. The validation only covers the accuracy in the estimation of the random error component associated with a linear measurement, when the proposed statistical modelling approach is adopted to represent random variability in the point cloud across measurement repeats. The validation does not cover the accuracy of the method at estimating bias, thus the test data used in this validation does not contain any bias component. The validation method consists of the following steps, also summarised in Figure 8.
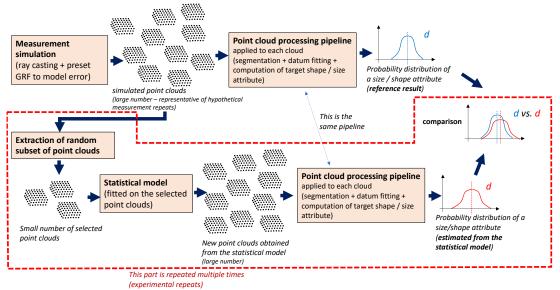

Figure 8. Validation procedure based on simulated measurements. The top row shows the process to obtain the reference result. The bottom row illustrates the estimation procedure implemented using statistical point cloud modelling.

Simulated measurements (Figure 8 – top left) are performed on digital, test geometries by combining ray casting (i.e. projecting a grid or rays onto a triangle mesh) and a GRF of known parameters to produce point clouds incorporating known random measurement error. An arbitrarily high number of point clouds

can be produced, representative of an ideal, but unrealistic scenario where one could perform a very large number (hundreds) of measurement repeats on the same test part. The point clouds are then processed (Figure 8 – top row) through a computational pipeline for shape/size inspection specifically devised for the test geometries and dedicated to computing selected shape or size attributes. As the same pipeline is applied to all the virtually generated point clouds, probability distributions for each targeted attribute can be obtained (Figure 8 – top right). As a large number of point clouds is used to obtain these probability distributions, they are selected as representative of the "ground truth" about measurement error (random error across repeats) for the selected test case. The results of this simulation represent the ideal characterisation result that our method aims to achieve.

A much smaller subset of point clouds is randomly extracted from the overall set of simulated measurement repeats, and used as the starting point for the application of the proposed method (Figure 8 – bottom left). Essentially, we are simulating a more realistic scenario where the user can only perform a limited number of measurement repeats, and has no additional knowledge of measurement error. The availability of three repeats (three point clouds) it typical, but we have also considered scenarios with five and ten repeats, although these are increasingly unrealistic possibilities in real inspection scenarios. Following the proposed method (Section 2.4 and Section 2.5), a new GRF is estimated from the available, small number of point clouds. Then new point clouds can be generated from the GRF (bottom centre of Figure 8). The GRF estimated from a small number of point clouds can only be an approximation of the unknown "ground truth". Still, the same reference pipeline for dimensional inspection is now applied to all the new point clouds generated by the approximated GRF, leading (again by Monte Carlo simulation) to estimated probability distributions for the selected size or shape attributes (Figure 8 – bottom right). Such probability distributions are compared with the ideal result (Figure 8 – middle right) to assess how closely the results of the proposed method match the ideal result (by comparison of the shape and statistics of the probability distributions).

The estimation process (Figure 8 – bottom row) is repeated multiple times, by randomly extracting a different subset of point clouds from the global set. The differences between the probability distributions of the estimated and reference results are assessed both via comparison of sample means and standard deviations, and via a nonparametric two-sample Kolmogorov-Smirnov (K-S) test [50]. The null hypothesis of the K-S test is that the two samples (in our case, the estimate and reference) belong to the same distribution. Hence, if the K-S test rejects the null hypothesis we can conclude that the estimation did not perform well (i.e. the estimated sample belongs to a distribution which is different from the "true" one). Finally, an investigation is carried out on how the choice of the number of point clouds used to estimate the GRF (Figure 8 – bottom left) affects the accuracy of the prediction (closeness between the results produced by the proposed approach and the reference results).

3. RESULTS

3.1. Generation of the simulated measurement repeats

Simulated measurement repeats were generated using test geometries for use in the validation method described in Section 2.9, thus with the sole objective of assessing accuracy in the estimation of random error components associated with linear dimensions (i.e. no bias).

A prismatic part (cuboid) and a cylindrical part were selected as virtual geometries. Measurement was simulated by first performing high-density ray casting from viewpoints at infinite distance (parallel rays), along multiple directions and by merging the resulting point clouds. The result of ray casting, a deterministic cloud, was then disturbed by adding a random scalar contribution to each point along its local normal. The random scalars were generated using a GRF with the following mean vector $\boldsymbol{\mu}$ and covariance matrix $\mathbf{K}$ functions:

$$\mu(\boldsymbol{p}_i) = 0, \qquad\qquad\qquad \forall(\boldsymbol{p}_i) \qquad\qquad\qquad (7)$$

$$k(\boldsymbol{p}_i, \boldsymbol{p}_j) = \sigma^2 exp\left(-\frac{dist(\boldsymbol{p}_i, \boldsymbol{p}_j)^2}{2l^2}\right), \qquad \forall(\boldsymbol{p}_i, \boldsymbol{p}_j) \qquad\qquad (8)$$

where the mean function $\mu(\boldsymbol{p}_i)$ is an all-zero function for each point $\boldsymbol{p}_i$ and the covariance function $k(\boldsymbol{p}_i, \boldsymbol{p}_j)$ between any pair of points $\boldsymbol{p}_i, \boldsymbol{p}_j$ is defined using a squared-exponential kernel. In the

covariance function, σ represents a constant variance term affecting all the points, $dist$ indicates the computation of the Euclidean distance between $\boldsymbol{p}_i$ and $\boldsymbol{p}_j$, and l is referred to as $lengthscale$, i.e. a reference distance to modulate the spatial extents of dependency between points. The choice of a zero mean function implies that no local bias was added to the measurement error (i.e. only random components). The squared exponential formulation for covariance was chosen to model spatial correlation as it is dependent on the relative distance between points, but not on their absolute location in the cloud (i.e. it is shift-invariant).

For the cuboid, the following parameters were adopted:

- size of the test part: (40 × 60 × 20) mm;
- size of the point cloud: ~5530 points (after stitching of two datasets taken from tilted, symmetrical viewpoints);
- standard deviation σ in the squared exponential kernel: 20 μm; and
- lengthscale l in the squared exponential kernel: 30 μm.

For the cylinder:

- size of the test part: 80 mm (diameter) × 100 mm (length);
- size of the point cloud: ~7570 points (after stitching of two datasets taken from tilted, symmetrical viewpoints);
- standard deviation σ in the squared exponential kernel: 20 μm; and
- lengthscale l in the squared exponential kernel: 30 μm.

The standard deviation (in the model, representative of local noise orthogonal to the surface) was chosen based on previous experimentation with multiple optical measurement technologies on additively manufactured parts (to be consistent with the real test case). The lengthscale was chosen based on the idea to consider spatial dependency the same order of magnitude of local noise. In Figure 9, an instance of simulated measurement is shown for the prismatic part and for the cylindrical part. A total of 200 instances (simulated point clouds) were generated for the cuboid, and another 200 for the cylinder.
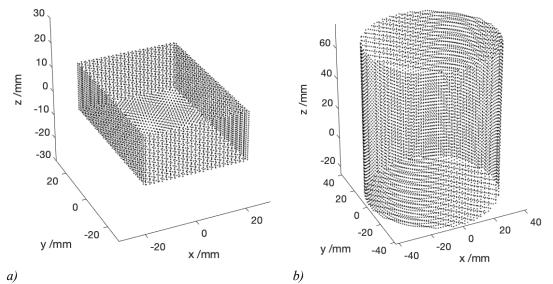

a)   b)

Figure 9. Example point clouds obtained on the test parts via simulated measurement; a) cuboid; b) cylinder.

3.2. The point cloud processing pipeline

Selected size attributes for the cuboid consisted of its three main features of size, aligned to the axes (x,y and z) of the Cartesian reference system and referred to as: dx, dy and dz in the following. For the cylinder, height (dz) and diameter ($diam$) were selected. A fully automated algorithmic pipeline was developed to compute the selected size attributes from each point cloud. The pipeline is similar for the cuboid and for the cylinder. First, the point cloud is partitioned into regions using the direction of the local normal

computed by principal component analysis (PCA) in combination with k-means clustering on the local normal (more information on the use of k-means clustering combined with local normal can be found in previous work [51]). For both the cuboid and the cylinder, k-means was performed with $k = 6$, in order to isolate "faces" oriented according to the main six directions (examples are shown in Figure 10). For the cylinder, this resulted in the lateral (cylindrical) surface being split into four regions.
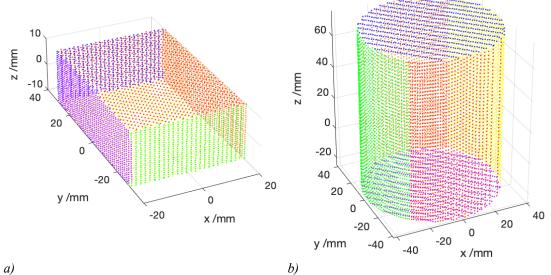

a)   b)

Figure 10. Example segmentation of the test point clouds; k-means on local normal; k = 6; a) cuboid, b) cylinder.

In the automated pipeline, to compute distances between pairs of nominally parallel faces (i.e. faces related to the computation of *dx*, *dy*, *dz* for the cuboid and *dz* for the cylinder), the surfaces of each pair were individually fitted to planar datum features using RANSAC and total least-squares. Then, one datum per pair was selected as primary, and the Euclidean distance between the datum centroid and the intersection with the other datum, computed along the direction of the local normal to the primary datum, was computed. The entire procedure is summarised in Figure 11.

a)   b)   c)
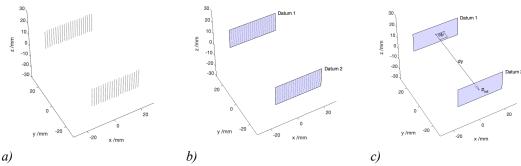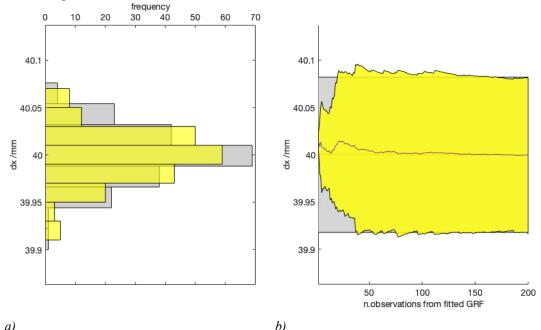
Figure 11. Procedure to automatically determine a linear dimension as the distance between two datum planes (in the example: linear dimension dy for the cuboid); a) the two point subsets resulting from segmentation of the original cloud (identified by the direction of the local normal) are isolated; b) the two subsets are independently fitted to datum planes; c) datum 1 is elected as primary, the datum centroid point (ctr) is obtained by projecting all the fitted points on their associated datum and computing the resulting two-dimensional centroid. A ray orthogonal to Datum 1 is drawn from the centroid to the intersection with the second datum (point p_{int}). The Euclidan distance between ctr and p_{int} is elected as the final result for the linear dimension.

A different method was devised to compute the diameter (*diam*) for the cylinder. In this case, a cylindrical datum feature was fitted (RANSAC and total least-squares) to the four lateral (curved) regions obtained by segmentation (see Figure 10.b), and the diameter of the datum was extracted as the result.

3.3. Results for the test parts

The procedure illustrated in Section 2.9 and Figure 8 was applied to the cuboid and cylinder point clouds in combination with the point cloud processing pipeline described in Section 3.2. First, a total of 200

observations for each targeted dimension (*dx, dy, dz* for the cuboid, *dz* and *diam* for the cylinder) were obtained (using the pipeline described in the top portion of Figure 8, thus by generating 200 reference point clouds), leading to the construction of a probability distribution for each. These distributions were considered as the reference results, i.e. representative of the "ground truth" targeted by the estimation proposed in this work. Statistical point cloud models were then generated following the approach described in Section 2.4 and Section 2.6 using random selections of three, five and ten point clouds extracted from the previously generated population set of 200 point clouds per type of geometry (cuboid, cylinder). New virtual clouds were then obtained from the fitted statistical models to reach to a final equivalent count of 200 new virtual clouds per geometry type (bottom portion of Figure 8). The same point cloud processing pipelines were applied to the virtual clouds in order to obtain new probability distributions, this time representing the estimation of the error associated with each targeted linear dimension. An example result is shown in Figure 12, representing the *dx* dimension of the test cuboid. The example result was obtained by building a statistical point cloud model starting from a random sample of three point clouds extracted from the pool of 200 (as illustrated by the data processing pipeline shown in Figure 8 bottom left).

a)   *b)*

Figure 12. Results for one simulation run for the dx parameter of the test cuboid; a) comparison between the histograms of the estimated distribution (yellow) and reference distribution (grey); b) evolution of the estimated distribution (yellow) in comparison to the reference one (grey) as an increasing number of point clouds generated by the statistical model is considered in the estimation. The yellow and grey bands refer to $\mu \pm 3\sigma$.

In Figure 12.a, the histogram of the final estimation result (yellow) for the cuboid *dx* (i.e. the result of the data processing pipeline shown in Figure 8 – bottom right) is overlaid on the histogram of the reference *dx* value (grey), i.e. the result of the data processing pipeline shown in Figure 8 – top right. The probability distribution of the final estimation was obtained by using 200 new observations sampled from the fitted statistical model (Figure 8 – bottom row), i.e. the same number of observations used to obtain the reference result. In the distribution shown in Figure 12.a, the signed difference between the estimated and reference means was -0.7 μm (-0.0017% of the reference value), and the signed difference between the estimated and reference standard deviations was 0.3 μm (1.07% of the reference standard deviation for *dx*).

For comparison, it is useful to look at the estimation result when no statistical point cloud model was used and no new observations were generated from it by Monte Carlo simulation. In this case, the mean and standard deviation of the diameter can be obtained directly from the three measurement repeats originally intended for fitting the statistical model. This corresponds to a scenario where dimensional properties are estimated directly from the few, real measurement repeats available. For the example shown in Figure 12, the signed difference between the estimated and reference means for *dx* was -8.6 μm, i.e. -0.02% of the reference mean (one order of magnitude larger than the result using the proposed approach), and the signed difference between the estimated and reference standard deviations for *dx* was

13.3 µm, i.e. 48.6% of the reference standard deviation (again one order of magnitude larger than the result using the proposed approach). The K-S test on the results shown in Figure 12 failed to reject the null hypothesis at 95% confidence level, indicating that there was not enough evidence to declare the two probability distributions (reference and estimated) as different.

In Figure 12.b a visual representation is provided to show how the estimated probability distribution evolves when an increasing number of new observations is drawn from the fitted statistical point cloud model (from two to 200). The yellow band indicates the mean $\pm 3\sigma$ of the estimated prediction, evolving towards the right of the plot as the number of observations increases. On the contrary, the grey band in Figure 12.a refers to the reference result (Figure 8 – top right), which is constant as it is always computed from 200 observations obtained by simulation. The upper and lower limits of the grey band correspond to $\mu \pm 3\sigma$. The central lines of the grey and yellow bands indicate the respective means.

For dx of the cuboid, the plots in Figure 12.b indicated that with very low numbers of observations, the estimate differs more significantly from the reference, but as the number of observations increases, it stabilises around the reference value. Interestingly, the K-S test failed to reject the null-hypothesis at the 95% confidence level in all cases, including when considering estimates produced from very few observations, indicating that there is no statistical evidence to say that the two probability distributions are different, even when visually the two distributions do indeed appear to differ (for low counts of observations). This latter result may hint at a low statistical power of the K-S test in its current configuration (but see Section 4).

The plots shown in Figure 12 refer to a single random sample of three point clouds drawn from the set of 200 and used to fit the statistical point cloud model. Similar outcomes were also obtained when fitting a statistical point cloud model using samples of five or ten point clouds (Figure 13). Ultimately, using three, five or ten observations to fit the GRF did not seem to make a significant difference in terms of the accuracy of the final estimates of mean and standard deviation. This is a likely a consequence of the sample size being, in all cases, very small compared to problem complexity ($\sim$5500 random variables in the GRF for the cuboid).

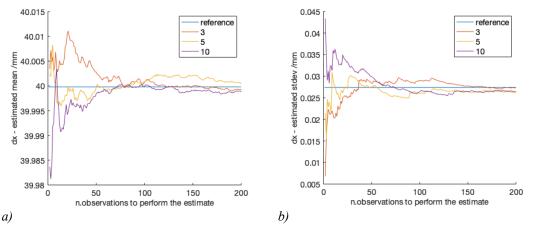*a)*   *b)*

Figure 13. mean (a) and standard deviation (b) of the cuboid dx dimension, evolving as an increasing number of observations are drawn from the statistical model (from two to 200). The plots compare the effects on estimation performance when choosing three, five or ten point clouds to fit the statistical model. In both plots, the straight horizontal line is the reference value.

The experiments with three, five and ten point clouds (bottom part of Figure 8) were repeated five times, each time drawing a new random subset of point clouds from the same pool of 200 to build the statistical model. Similar trends were observed. The entire set of results obtained for the two test geometries and all the selected features of size is summarised in Table 1 (cuboid) and Table 2 (cylinder). All the individual values reported in the table are arithmetic means of the five consecutive experiments. All estimates are computed on 200 new point clouds drawn from the statistical models.

Table 1. Results for dimensions of the cuboid test geometry: "reference" is the reference value for the related statistics (mean or standard deviation); "n.sel" is the number of point clouds selected to fit the GRF (representative of a scenario where one may have that number of point clouds from measurement repeats); "estimate from sel" refers to computing the statistics on the linear dimension using solely the selected point

cuboid		reference /mm	n.sel	estimate from sel /mm	error /µm	error /%	estimate from stat model /mm	error /µm	error /%	reduction of estimation error (stat model vs sel) / µm
dx	mean	40.000	3	40.005	4.915	0.01%	39.999	-0.413	0.00%	4.502
			5	40.007	6.924	0.02%	40.000	0.157	0.00%	6.767
			10	39.998	-2.160	-0.01%	40.001	1.245	0.00%	0.915
dx	std	0.027	3	0.029	1.208	4.41%	0.027	-0.454	-1.66%	0.754
			5	0.029	1.139	4.16%	0.027	-0.273	-1.00%	0.866
			10	0.027	-0.148	-0.54%	0.027	-0.591	-2.16%	-0.443
dy	mean	59.997	3	60.004	6.855	0.01%	60.000	2.593	0.00%	4.262
			5	59.999	1.533	0.00%	60.000	2.523	0.00%	-0.990
			10	60.005	7.295	0.01%	59.998	0.924	0.00%	6.371
dy	std	0.027	3	0.019	-7.919	-29.22%	0.027	-0.084	-0.31%	7.835
			5	0.023	-3.877	-14.30%	0.027	0.301	1.11%	3.576
			10	0.027	-0.391	-1.44%	0.027	-0.185	-0.68%	0.206
dz	mean	20.000	3	20.004	3.712	0.02%	19.999	-1.221	-0.01%	2.491
			5	20.001	1.331	0.01%	20.000	-0.181	0.00%	1.151
			10	20.003	3.033	0.02%	19.999	-1.229	-0.01%	1.804
dz	std	0.029	3	0.028	-1.160	-3.98%	0.031	1.553	5.33%	-0.393
			5	0.027	-2.387	-8.19%	0.033	3.502	12.01%	-1.114
			10	0.025	-3.660	-12.56%	0.031	2.052	7.04%	1.609

Table 2 Results for the features of size of the cylinder test geometry. For a reading guide, see Table 1.

cylinder		reference /mm	n.sel	estimate from sel /mm	error /µm	error /%	estimate from stat model /mm	error /µm	error /%	reduction of estimation error (stat model vs sel) / µm
diam	mean	80.046	3	79.876	-170.586	-0.21%	79.999	-47.447	-0.06%	123.138
			5	79.971	-75.248	-0.09%	80.010	-36.049	-0.05%	39.199
			10	79.986	-60.695	-0.08%	80.007	-38.839	-0.05%	21.856
diam	std	0.397	3	0.241	-156.360	-39.37%	0.376	-21.606	-5.44%	134.754
			5	0.491	93.974	23.66%	0.367	-29.938	-7.54%	64.036
			10	0.399	1.395	0.35%	0.336	-61.568	-15.50%	-60.173
dz	mean	100.000	3	99.995	-5.572	-0.01%	100.002	1.237	0.00%	4.335
			5	100.008	7.085	0.01%	100.000	-0.521	0.00%	6.564
			10	100.006	5.740	0.01%	100.001	0.753	0.00%	4.987
dz	std	0.027	3	0.014	-13.125	-48.54%	0.027	-0.340	-1.26%	12.785
			5	0.017	-10.496	-38.81%	0.027	-0.195	-0.72%	10.301
			10	0.023	-3.805	-14.07%	0.027	-0.244	-0.90%	3.561

As shown in Table 1 and Table 2, the estimates obtained by using the proposed approach (Monte Carlo simulation using the statistical point cloud model) are almost always more accurate than simply estimating the statistics using only the available observation repeats. It is interesting to look at the confidence intervals associated with the estimations, i.e. the confidence intervals associated with the columns "estimate from sel" and "estimate from stat model".
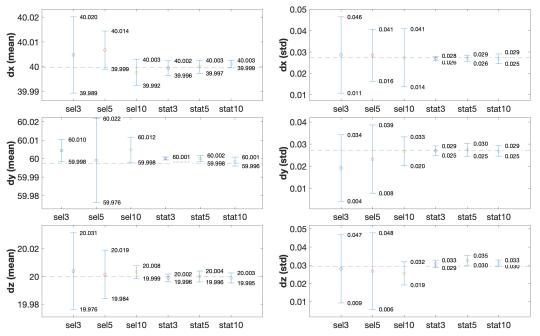
Figure 14. Analysis of the confidence intervals (Cis) associated to the estimates for the cuboid test case. All values are in mm, CIs are computed at 95% confidence on means of five simulation repeats. In each panel, the gray dashed, horizontal line represent the reference mean statistics (i.e. the "truth"). The CIs with labels 'sel3','sel5' and 'sel10' refer to estimates performed directly on the sets of 3, 5 or 10 selected point clouds. The labels 'stat3','stat5' and 'stat10' refer to estimates performed on 200 point clouds generated from the statistical models fitted over 3, 5 or 10 point clouds. All the panels in the left column report estimates of the mean statistics of the selected linear dimension (i.e. the confidence interval on the mean of the means). The panels in the right column report the confidence intervals on the mean of the standard deviations.
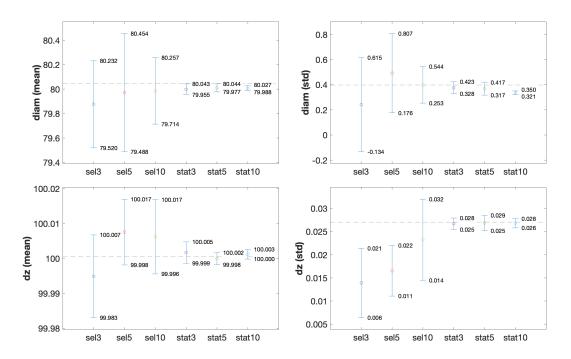

Figure 15. Analysis of the confidence intervals of the estimations for the cylinder test case. For a reading guide, refer to Figure 14.

From Figure 14 and Figure 15, clearly the CIs computed directly on the selected point clouds are much wider, given the very small sample sizes (3, 5 and 10 respectively). On the contrary, all the CIs associated with estimates from point clouds generated by the statistical models are much narrower, having been

obtained from 200 point clouds each. The middle point of each CI is the mean of the estimate, i.e. the same value reported in Table 1 and Table 2 under the columns "estimate from sel" and "estimate from stat model". The results reported in Figure 14 and Figure 15 confirm the advantage of using the statistical model to obtain an estimate of the statistics of the linear dimension (mean and standard deviation) generally both more accurate (closeness of the mean to the reference "truth") and more precise (narrow confidence interval) compared to simply relying on the available measurement repeats. The size of the sample (number of point clouds) used to build the statistical model does not seem to have a clear influence on the results, with no visible trends going from three to ten. As stated earlier, this is a likely indication that sample size is very small regardless, given the number of random variables involved in the model ($\sim$5500 for the cuboid, $\sim$7500 for the cylinder). The choice of selecting 3, 5 or 10 point clouds is consistent with industrial applicability of the proposed approach, if the sample is assumed as available from measurement repeats.

Finally, it is useful to report information about computational requirements of the procedure applied to the simulated test cases. A full validation run (one repeat), covering two test geometries, GRFs fitted on 3, 5 or 10 point clouds, with 200 new point clouds generated as reference for each case, and another 200 point clouds generated to assess the estimation performance of the GRF took approximately 16 hours on a mid-speed personal computer (4 core 2.8 GHz Intel Core i7, with 16 Gb RAM), resulting in approximately 15 Gb of data. In the intended usage scenario, i.e. where one would select a number of observations from one geometry, fit the statistical model on such point clouds and then generate 200 new point clouds to perform estimations via Monte Carlo simulation, the current implementation would require a litte more than one hour of computing time, generating approximately 1.5 Gb of data, the biggest culprit being the estimation and storage of the covariance matrix. As the current implementation is in prototype form and designed to act solely as proof-of-concept, performance can be improved, for example by using parallelisation.

3.4. Application to a real test case

While the purpose of the simulated test case was to determine how closely the estimated distribution of a target dimension would match the reference (as a measure of accuracy of the method in a test case with known "truth"), the purpose of the real test case is to show how results from the method can be used to gain insight into the metrological performance of a real measurement.

A measurement test artefact was developed [52], based on a previous design by the National Institute of Standards and Technology (NIST) [53]. The test artefact is sized (50 × 50 × 28) mm (size of the enclosing envelope) and was fabricated in Ti-6Al-4V using laser powder bed fusion (Figure 16.b).

a)   b)
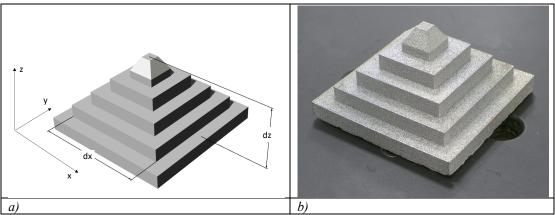
Figure 16. Selected test part (pyramid artefact); a) CAD model, indicating also the features of size selected for the characterisation (see Section 3.5); b) Ti-6Al-4V sample fabricated by laser powder bed fusion.

The test artefact was measured using a commercial fringe projection system (GOM ATOS Core 300 [54]). Three measurement repeats were performed, resulting in raw point clouds of approximately 100,000 points. A second high-density measurement was taken using a contact CMS (Mitutoyo Crysta Apex S7106 with a ST25 probe [55]) to act as a nominally more accurate reference. For tactile measurement, scanning mode was used with 10 μm spacing between consecutive points in a scan line,

and 200 µm spacing between parallel scanlines. The contact-CMS measurement was repeated three times.

The optical and contact point clouds were processed in CloudCompare [56]. The point clouds were first registered to the available CAD model (triangle mesh in STL format) using a coarse alignment method based on manual point determination to establish correspondences, followed by fine alignment by iterative closest points (ICP) [57]. The point clouds were then reduced in size (pre-processing) to contain the computational complexity in the estimation of the covariance matrix. Size reduction was performed by resampling to achieve a target spacing between points, using the grid average method [58]. The point spacing was set at 0.5 mm as a compromise between cloud density and the need for preserving the integrity of the part edges. The resampled point clouds from optical measurement contained approximately 12,000 points each (see example in Figure 17.a), while the resampled clouds from contact CMS measurement contained approximately 85,000 points each (Figure 17.b). Point normals were computed by locally fitting quadric surfaces to the point cloud [59]; normal orientations were fixed (so that they would point outwards) by using the minimum spanning tree method [60].
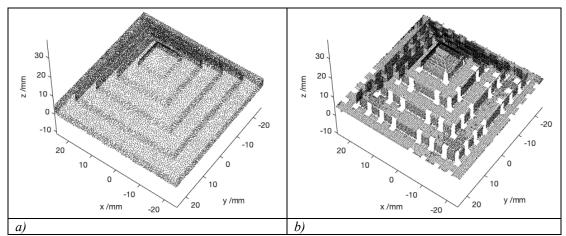

Figure 17. Example point clouds obtained from measurement of the pyramid artefact (after resampling); a) optical; b) contact CMS (visible gaps are non-measured regions to avoid collisions with the probe).

3.5. The point cloud processing pipeline

Two dimensions (dx and dz, aligned to the x and z axes respectively) were selected as the target attributes (see Figure 16.a). The dimension dx refers to the distance between parallel walls measured at the first "step" of the pyramid, aligned to the x axis. The dimension dz refers to the vertical (i.e. along the z axis) distance between the top surface of the pyramid and the surface of the first step. The same point cloud processing pipeline was applied to all the optical and contact-CMS clouds. The pipeline consisted of the following steps: the point cloud was first partitioned using the signed direction of the local normal computed by PCA in combination with k-means clustering (see Figure 18.a and Figure 18.b). Clustering was performed with $k = 5$ in order to compensate for the lack of points on the bottom surface (negative z orientation). Then each region was recursively split into subregions by running another k-means clustering operation based on point placement along the axis identified by the direction associated to the cluster. So, for example, the region associated to the $x+$ direction was split into five sub-clusters to accommodate for the presence of five surfaces along the $x+$ axis. To compute the dimensions dx, dy and dz, regions were fitted to planes and paired, then the distance between the centroid of a fitted plane and the other fitted plane was computed as the target attribute.
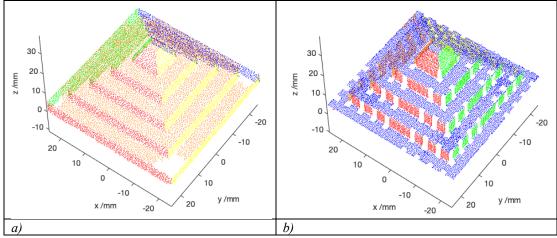
Figure 18. Results of the first segmentation step on the point clouds (k-means on local normals); a) optical; b) contact CMS.

3.6. Results for the real test case

Results for the targeted features of size dx and dz are shown in Figure 19 and Figure 20. In both figures:

- the black line represents the value of the targeted dimension, as the mean of three values obtained from the three contact CMS repeats. In the right panels of Figure 19 and Figure 20 the line appears as particularly bold because it is representing a band interval for uncertainty on the contact CMS value (see later in this section and Figure 21);
- the red line represents the value of the same dimension, obtained by the statistical model, via Monte Carlo simulation over the optical repeats (final value after 200 repeats in the left part of the figures, evolution using from two to 200 repeats in the right part).

The distance between the red and black line is the signed bias of the optical instrument with respect to the contact CMS (for the selected dimension). Bias can be mathematically expressed both as a signed distance and as a signed distance percentage, for example, for the target dimension dx:

$$bias\big(dx_{opt}, dx_{cms}\big) = \overline{dx}_{opt} - \overline{dx}_{cms}, \qquad bias\%\big(dx_{opt}, dx_{cms}\big) = \frac{\overline{dx}_{opt} - \overline{dx}_{cms}}{\overline{dx}_{cms}} \cdot 100 \qquad (9)$$

where the bar indicates the arithmetic mean and the subscript indicates optical or tactile CMS measurement, and where the results of the optical pipeline refer to the 200 observations extracted from the statistical model. Optionally, it is possible to add the uncertainty of the CMS to the above result: in absence of a comprehensive metrological characterisation of the CMS, it is possible to rely on the maximum permissible error (MPE) [61]) specified by the manufacturer to compute the standard uncertainty $u_{MPE} = MPE/\sqrt{3}$ MPE for the tactile CMS, thus:

$$bias\big(dx_{opt}, dx_{cms}\big) = \big(\overline{dx}_{opt} - \overline{dx}_{cms} \pm MPE/\sqrt{3}\big) \qquad (10)$$

The uncertainty is overestimated as it refers to a single CMS measurement, whilst the reference result ($\overline{dx}_{cms}$ in the example) is the mean of three repeats. Any bias falling within the uncertainty band of the CMS would not be appreciable when using the CMS measurement as a reference. Stated otherwise, the CMS would not be a sound reference to assess the bias of the optical measurement when bias is smaller than the known uncertainty of the CMS.

For the test pyramid, using the maximum permissible scanning probing error [62] as reported by the manufacturer of the CMS (MPE_THP = 2.2 µm), the results were:

$$bias\big(dx_{opt}, dx_{cms}\big) = (-48.53 \pm 1.27)\mu m \ (-0.12 \pm 0.03)\% \qquad (11)$$
$$bias\big(dz_{opt}, dz_{cms}\big) = (30.79 \pm 1.27) \ \mu m \ (0.13 \pm 0.04)\% \qquad (12)$$

i.e. the biases where approximately one order of magnitude larger than the CMS uncertainty. In Figure 21, a zoomed-in version of Figure 19.a is shown, highlighting the uncertainty band built around the CMS value using $\pm MPE/\sqrt{3}$.

The yellow bands surrounding the optical measurements, visible in Figure 19 and Figure 20, are an indication of the estimated precision in the computation of the dimension using optical measurement (i.e. random error in repeatability/reproducibility conditions) and are plotted in the interval $\overline{dx}_{opt} \pm 3s_{dx,opt}$ where $s_{dx,opt}$ is the standard deviation estimated for the dimension (dx in the example) using the optical observations (200 datasets obtained from the statistical model). The other plotted band (grey) represents the precision of the CMS assessed using three repeats, i.e. $\overline{dx}_{cms} \pm 3s_{dx,cms}$. For the pyramid test case, the results indicate higher precision for the CMS with respect to the optical system, as expected.

In quantitative form, the discrepancy between the standard deviations can be expressed as a signed difference: $s_{dx,opt} - s_{dx,cms}$, or as a signed difference percentage: $(s_{dx,opt} - s_{dx,cms})/s_{dx,cms}$, leading to 51.3 µm (214%), i.e. slightly more than double the scatter in the optical result, compared to the CMS.
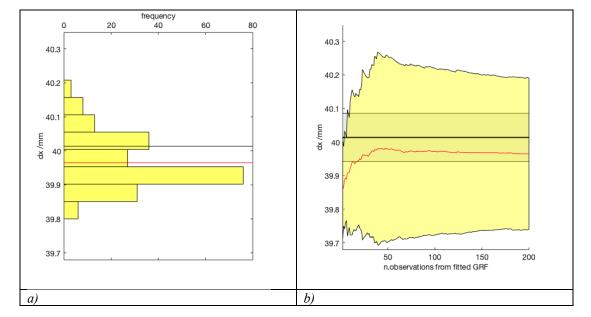

Figure 19. Results for the pyramid dimension: dx; a) histogram of the estimated distribution (yellow) with mean value (red line) compared to reference CMS result (black line); b) evolution of the estimated distribution (yellow) in comparison to the reference one (grey) as an increasing number of point clouds generated by the statistical model is considered in the estimation. The reference CMS result appear bolder because it is actually an interval ($\pm MPE/\sqrt{3}$) compressed as an effect of low magnification.
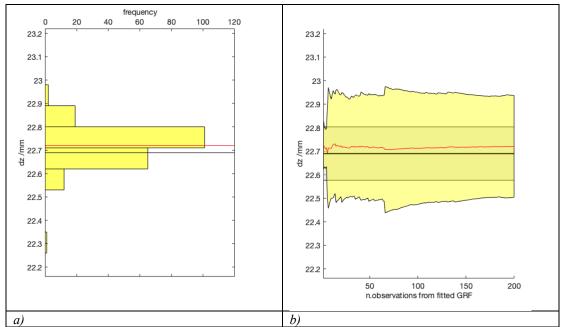
Figure 20. Results for the pyramid dimension dz; a) histogram of the estimated distribution (yellow) with mean value (red line) compared to reference CMS result (black line); b) evolution of the estimated distribution (yellow) in comparison to the reference one (grey) as an increasing number of point clouds generated by the statistical model is considered in the estimation. Other details as in Figure 19.
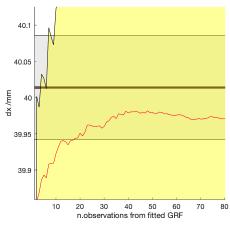

Figure 21. Zoomed in view of Figure 19.b to show the uncertainty band around the CMS value for dx (in red)

3.7. Spatial maps of bias and variance

In addition to estimating the probability distribution of features of size, the main advantage of having a statistical model of the point cloud itself is that more detailed information can be obtained about the nature of random error in correspondence to specific regions of the measured geometry. Spatial maps of bias can also be obtained, as long as either a reference measurement of stated uncertainty is available or a mathematical model is available to compute local bias, as discussed in Section 2.8. For the pyramid test case, where optical and CMS measurements are available, starting from the two GRFs generated from the measurements, spatial maps of local bias and local variance can be produced (Figure 22).
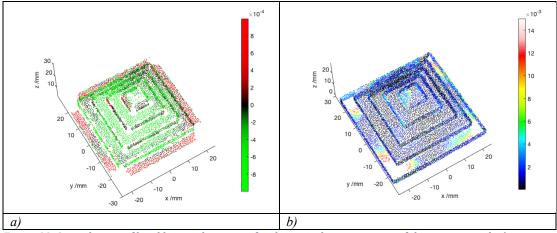
Figure 22. Spatial maps of local bias and variance for the optical measurement of the test pyramid; a) mean point cloud from the optical GRF coloured according to local bias (using the CMS GRF as reference). The map is produced only for those regions where the CMS data is available; b) mean point cloud from the optical GRF coloured according to local variance (using optical GRF only). Bias and variance values (both reported in mm) have been truncated to allow for better visualisation of smaller differences.

Spatial maps, such as those shown in Figure 22, can be useful to investigate instrument behaviour and performance in correspondence to specific form features on the measured part. For example, the observation of the spatial distribution of bias (Figure 22.a) indicates that the optical measurement is positively biased at the bottom-most step of the pyramid, as well as in some of the tilted areas near the top of the pyramid. In the middle regions, bias appears to be consistently negative. The observation of Figure 22.b (map of local variances for the optical GRF) shows higher variance in the measurement, again in correspondence to the base region of the pyramid. Because the specimen (Figure 16) shows a clear warping at the base level (a consequence of known shape bending often observed in Ti6Al4V parts fabricated by laser-powder bed fusion [63]), one may consider whether such a deformation may be responsible for both the observed bias and variance-related phenomena, a consideration worth further investigation.

4. DISCUSSION

A number of observations can be made about the results. Let us start from the simulated test case, which essentially illustrates the performance of the proposed approach for estimating the distribution of the targeted dimensions as a random variable. The first consideration is that choosing to *not* use the model, and instead attempting to directly estimate the dispersion of a dimension through the analysis of a few measurement repeats, is normally not a sound idea and can result in large estimation error. This finding is reasonable from a statistical point of view, when one considers that we are attempting to estimate the result of a non-linear transform (i.e. a dimension) starting from only a few observations (three, five, ten) of a multivariate random variable with 10,000 to 85,000 dimensions (size of the point cloud). On the other hand, generating a large number of observations via physical measurement repeats is clearly resource-prohibitive, which is why we normally rely on only a few physical repeats. On the contrary, the proposed approach, based on the estimation of a statistical model of the point cloud, provides an appealing solution to overcoming the costs of the repeats, by generating a large number of new, virtual observations without the need for further measurement.

Once the decision as to whether to generate a statistical model for the point cloud is taken, fitting the model on three, five or ten observations does not seem to make a large difference. This is presumably due to the same reasons mentioned above, i.e. three, five or ten are small numbers regardless, considering the size of the point cloud. It is, therefore, likely that performance of the statistical model may improve when the model is fit on 100+ or 1000+ observations. However, following such a route is not appealing, considering that there is little to no likelihood that such a high number of measurement repeats might ever be possible in a realistic environment, not to mention the added challenges due to likely presence of drift effects.

Another consideration arising in particular from the results of the simulated test case, is that the Kolmogorov-Smirnov non-parametric test cannot be reliably used to explain the differences between the estimated probability distribution of the dimension and the reference. This is presumably due to the low statistical power of the test (i.e. high probability of type II statistical error), which is again reasonable when considering that the null hypothesis (the two samples are drawn from the same distribution) may be difficult to reject when the distributions appear very similar (though we know from validation that they are ultimately different). Conversely, comparison based on moments of the distributions provides a better indication of differences and, for the simulated test case, was consistently able to provide a reliable quantification of differences. In addition to computing mean and standard deviation, higher order moments, such as skewness and kurtosis, could have been computed in order to refine the comparison. However, the computation of higher order moments was not deemed necessary as the priority was to assess differences in central tendency (mean) and dispersion (variance), though future studies may focus on targeting more comprehensive comparisons of shape.

The observation of the results obtained for the real test cases highlights the central role of bias, as a fundamental component of measurement error. In a real measurement scenario, when a single GRF is fitted to a series of repeats from the same instrument, our solution can only be used to estimate the dispersion associated to a dimension, but cannot provide an indication of bias. However, it was shown that when it is possible to rely on a more accurate additional set of measurements, bias can be estimated and ultimately combined to the predicted dispersion, thus providing an overall more complete depiction of measurement error. Alternatively, a separate mathematical model capable of producing bias information mapped to each location of part geometry may be combined with the proposed approach. This second route is evidently more appealing in particular for all those circumstances where an additional measurement may not be viable, but requires further research as the generation of a bias-estimation model is far from straightforward, as demonstrated by current literature on the subject, as previously illustrated in Section 1.

Ultimately, by using the proposed statistical modelling approach, it is possible to obtain a detailed depiction of random measurement error (in repeatability or reproducibility conditions, depending on how the repeats are taken), and optionally bias if a second set of more accurate measurements, or a separate prediction model, is provided. Information on measurement error may be obtained for a targeted dimension, via Monte Carlo simulation, or for the entire point cloud, because information on how dispersion and bias vary locally over the surfaces of the measured part is provided.

Is this result useable as an uncertainty? In our opinion, not directly. The whole idea of uncertainty is to provide numbers that one can associate with a single result for a dimension, or to a single point cloud. The goal of uncertainty is also to provide numbers that are as much as possible valid in any measurement scenario, and thus also part-independent. On the contrary, the need for having measurement repeats, the need for having also a second set for bias, and the fact that ultimately the results are valid only for the specific test case and only for the conditions the repeats have been obtained in, somewhat contradicts the purpose of uncertainty.

Nevertheless, we do believe that the proposed approach has merit, in particular in relation to two main aspects. Firstly, the approach provides a new means to investigate how measurement error is spatially mapped to all the regions of any given part: spatial detail on bias and precision can help shed light on the behaviour of a measurement solution in correspondence to specific types of surface features (flat, curved, step-like, high aspect-ratio, smooth, irregular, etc.) paving the way for the discovery of globally valid correlations that allow a valid uncertainty budget to be established. Secondly, the proposed procedure is well versed to be fully automated.

Our method paves the way for the development of "smart" measurement systems capable of performing self-assessment of measurement quality while in operation, and subsequently capable of autonomously performing corrective actions in order to improve the final quality of the measurement result. The idea is that a smart measurement system should be able to autonomously build the statistical model from a set of repeated measurements (which is already possible, as the model building step is fully automated) and use such model to a) construct a map of local bias and variance to serve as guidance to assess where measurement performed better and where it performed worse, in order to plan further measurement actions; b) estimate error associated to linear dimensions, and thus assess reliability of each in a part inspection scenario. The development of smart measurement systems relying on the statistical model presented in this work is currently explored as part of ongoing research work [64].

More complex is the idea of possibly merging point clouds belonging to measurements on different parts coming from the same production line. Clearly, in such a case the fitted statistical model would also include manufacturing variability between instances, and the discrimination of measurement-related error would be more challenging, with a larger number of currently unsolved issues. The possibility of adapting our method to operate on measurements of multiple part instances is currently evaluated as tentative candidate for future work.

5. CONCLUSIONS

In this work, an approach was presented to fit high-density point clouds obtained from measurement repeats into statistical point cloud models based on Gaussian random fields. The use of fitted fields and Monte Carlo simulation to estimate the probability distributions for features of size was demonstrated, as well as the possibility to generate spatial mappings of point dispersion and the combination with a second random field obtained from a nominally more accurate instrument (or accurate instrument model) as a means to estimate local bias. The use of fitted fields to create spatial maps describing local properties of the measurement (for example, local variance and local bias) was also illustrated. Future work on random fields involves further investigation into different methods to estimate mean and covariance in the random field, and the analysis of the consequences of choosing different interpolation and normal projection strategies when aggregating observations (individual point clouds), as well as an investigation on the effects of geometric registration. Future work will also undertake a more thorough investigation of the incorporation of mathematical models to predict local bias to remove the need for additional measurements with supposedly more accurate instruments. Finally, future work on the estimation of uncertainty will address the possibility to use the methods presented here as a starting point to infer more general behaviour of measurement solutions when confronted with specific surface features.

Acknowledgments

REFERENCES

[1]   Evans C J 2010 Certification, self-calibration, and uncertainty in testing optical flats *Proc. SPIE* **7656** 76560S

[2]   Fang F Z, Zhang X D, Weckenmann A, Zhang G X, Evans C 2013 Manufacturing and Measurement of Freeform Optics *Ann. CIRP* **62** 823-846

[3]   Brinksmeier E, Karpuschewski B, Yan J, Schönemann L 2020 Manufacturing of multiscale structured surfaces *CIRP Ann. in press*

[4]   Stavroulakis P I, Leach R K 2016 Invited review article: Review of post-process optical form metrology for industrial- grade metal additive manufactured parts *Rev. Sci. Instrum.* **87** 041101–52009

[5]   Leach R K, Bourell D, Carmignato S, Donmez A, Senin N, Dewulf W 2019 Geometrical metrology for metal additive manufacturing *Ann. CIRP* **68** 677-700

[6]   Oakland J, Oakland R 2019 *Statistical Process Control*, 7th edn (Routledge)

[7]   Burdick R K, Borror C M, Montgomery D C 2005 *Design and Analysis of Gauge R&R Studies: Making Decisions with Confidence Intervals in Random and Fixed ANOVA Models* (*Series on Statistics and Applied Probability* vol 17) (Philadelphia: SIAM)

[8]   Blokdyk G 2020 *Measurement System Analysis A Complete Guide* (Emereo Pty Ltd)

[9]   Carmignato S, Voltan A, Savio E 2010 Metrological performance of optical coordinate measuring machines under industrial conditions *Ann. CIRP* **59** 497-500

[10]   Catalucci S, Senin N, Sims-Waterhouse D, Ziegelmeier S, Piano S, Leach R 2020 Measurement of complex freeform additively manufactured parts by structured light and photogrammetry *Measurement* **164** 108081

[11]   Mathys A, Brecko J, Semal P 2013 Comparing 3D digitizing technologies: What are the differences? *IEEE DigitalHeritage, Marseille, France* **1** 201-204

[12]   Leach R, Haitjema H 2010 Bandwidth characteristics and comparisons of surface texture

measuring instruments *Meas. Sci. Technol.* **21** 079801

[13] Ferrucci M, Haitjema H, Leach R K 2018 Dimensional metrology. In: Leach R K, Smith S T *Basics of Precision Engineering* (CRC Press: New York)

[14] Rivas Santos V M, Thompson A, Sims-Waterhouse D, Maskery I, Woolliams P, Leach R K 2020 Design and characterisation of an additive manufacturing benchmarking artefact following a design-for-metrology approach *Addit. Manuf.* **32** 100964

[15] Lou S, Brown S B, Sun W, Zeng W, Jiang X, Scott P J 2019 An investigation of the mechanical filtering effect of tactile CMM in the measurement of additively manufactured parts *Measurement* **144** 173-182

[16] Gayton G, Su R, Leach R K, Bradley-Smith L 2019 Uncertainty evaluation of fringe projection based on linear systems theory *Proc. 35th CMSC, Orlando, USA*

[17] Sims-Waterhouse D, Isa M, Piano S, Leach R K 2019 Uncertainty model for a traceable stereo-photogrammetry system *Prec. Eng.* **63** 1-9

[18] ISO/DIS 10360 part 13 2020 *Geometrical product specifications (GPS) - Acceptance and reverification tests for coordinate measuring systems (CMS) - Part 13: Optical 3D CMS* (International Organization for Standardization)

[19] VDI/VDE 2634 Part 3 2014 *Optical 3D-measuring systems - multiple view systems based on area scanning*

[20] ISO 15530 part 3 2011 *Geometrical Product Specifications (GPS) – Coordinate measuring machines (CMM): Technique for determining the uncertainty of measurement - Part 3: Use of calibrated workpieces or measurement standards* (International Organization for Standardization)

[21] ISO/TS 15530 part 4 2008 *Geometrical Product Specifications (GPS) – Coordinate measuring machines (CMM): Technique for determining the uncertainty of measurement - Part 4: Evaluating task-specific measurement uncertainty using simulation* (International Organization for Standardization)

[22] Balsamo A, Di Ciommo M, Mugno R, Rebaglia B I, Ricci E, Grella R 1999 Evaluation of CMM Uncertainty through Monte Carlo simulations *Ann. CIRP* **48** 425-428

[23] Flack D 2013 Measurement Good Practice Guide No. 130 Co-ordinate measuring machine task-specific measurement uncertainties (National Physical Laboratory: London)

[24] Coupland J, Nikolaev N 2020 Surface scattering and the 3D transfer characteristics of optical profilometers *Proc. SPIE* **11352**

[25] Zhang B, Davies A, Evans C, Ziegert J 2018 Validity of the instrument transfer function for fringe projection metrology *Appl. Opt.* **57** 2795-2803

[26] Leach R K 2014 *Fundamental Principles of Engineering Nanometrology* 2nd edn (Binghamton: Elsevier Science)

[27] De Chiffre L, Carmignato S, Kruth J P, Schmitt R, Weckenmann A 2014 Industrial applications of computed tomography *Ann. CIRP* **63** 655-677

[28] Pauly M, Mitra N J, Guibas L 2004 Uncertainty and variability in point cloud surface data *SPBG'04, Goslar, Germany* 77-84

[29] Forbes A B 2006 Surface fitting taking into account uncertainty structure in coordinate data *Meas. Sci. Technol.* **17** 553-558

[30] Forbes A B 2006 Uncertainty evaluation associated with fitting geometric surfaces to coordinate data *Metrologia* **43** 282-290

[31] Forbes A B, Minh H D 2011 Form assessment in coordinate metrology *Appr. Alg. Complex Syst. Springer Proc. Math.* **3** 69-90

[32] Zhang M, Anwer N, Mathieu L, Zhao H B 2011 A discrete geometry framework for geometrical product specifications *Proc. CIRP Design Conf., Korea*

[33] Zhang M, Anwer N, Stockinger A, Mathieu L, Wartzack S 2013 Discrete shape modeling for skin model representation *P. I. Mech. Eng. B-J. Eng.* **227** 672-680

[34] Anwer N, Ballu A, Mathieu L 2013 The skin model, a comprehensive geometric model for engineering design *Ann. CIRP* **62** 143-146

[35] Thompson A, Senin N, Giusca C, Leach R K 2017 Topography of selectively laser melted surfaces: a comparison of different measurement methods *Ann. CIRP* **66** 543-546

[36] Evans C J 2008 Uncertainty evaluation for measurements of peak to valley surface form errors *Ann. CIRP* **57** 509-512.

[37] Evans C, Davies A 2013 Certification, self-calibration and uncertainty in optical surface testing *Int. J. Precis. Technol.* **3** 388-401

[38] Moroni G, Syam W P, Petrò S 2018 A simulation method to estimate task-specific uncertainty in 3D microscopy *Measurement* **122** 402-416

[39] Yang T H, Jackman J 2000 Form error estimation using spatial statistics *J. Manuf. Sci. Eng. Trans. ASME* **122** 262-272

[40] Fei L, Dantan J Y, Baudouin C, Du S 2019 Calibration and uncertainty estimation of non-contact coordinate measurement systems based on Kriging models *Prec. Eng.* **57** 16-29

[41] Ozendi M, Akca D, Topan H 2016 An empirical point error model for TLS derived point clouds *ISPRS Archives* **XLI-B5** 557-563

[42] Chen X, Zhang G, Zhang J, Wu H, Lu T, Xuan W 2016 An average error ellipsoid model for evaluating precision of point cloud from TLS *J. Ind. Soc. Remote Sens.* **44** 865-873

[43] Du Z, Wu Z, Yang J 2016 Error ellipsoid analysis for the diameter measurement of cylindroid components using a laser radar measurement system *Sensors* **16** 714

[44] Du Z, Wu Z, Yang J 2016 Point cloud uncertainty analysis for laser radar measurement system based on error ellipsoid model *Opt. Laser Eng.* **79** 78-84

[45] Rasmussen C E, Williams C K I 2018 *Gaussian Processes for Machine Learning* (Cambridge, Massachusetts: The MIT Press)

[46] Cressie N A C 2015 *Statistics for Spatial Data, Revised Edition* (John Wiley & Sons, Inc.)

[47] Genton M G 2002 Classes of kernels for machine learning: a statistics perspective *J. Mach. Learn. Res. – JMLR* **2** 303-304

[48] Senin N, Thompson A, Leach R K 2017 Characterisation of the topography of metal additive surface features with different measurement technologies *Meas. Sci. Technol.* **28** 095003

[49] Chen Y, Wiesel A, Eldar Y C, Hero A O 2010 Shrinkage algorithms for MMSE covariance estimation *IEEE Trans. Signal Process.* **58** 5016-5029

[50] Massey F J 1951 The Kolmogorov-Smirnov test for goodness of fit *J. Am. Stat. Assoc.* **46** 68-78

[51] Catalucci S, Senin N 2020 State-of-the-art in point cloud analysis. In: Leach R K *Advances in Optical Form and Coordinate Metrology* (IOP Publishing), Chap. 2

[52] Sims-Waterhouse D, Bointon P, Piano S, Leach R K 2017 Experimental comparison of photogrammetry for additive manufactured parts with and without laser speckle projection *Proc. SPIE* **10329**

[53] Moylan S, Slotwinski J, Cooke A, Jurrens K, Donmez M A 2012 Proposal for a standardized test artifact for additive manufacturing machines and processes *Addit. Manuf. Conf. SFF, Austin, Texas*

[54] GOM Atos Core 300 https://www.gom.com/metrology-systems/atos/atos-core.html

[55] Mitutoyo Crysta Apex S7106 CMM http://mitutoyo.co.uk/

[56] Girardeau-Montaut D C 2019 CloudCompare v2.11 beta (Anoia) [64bit]. Available online: https://www.danielgm.net/cc. Last accessed: 3rd April 2020

[57] Besl P, McKay N 1992 A method for registration of 3-D shapes *IEEE Trans. Pattern Anal. Mach. Intell.* **14** 239-256

[58] Pauly M, Gross M, Kobbelt L P 2002 Efficient simplification of point-sampled surfaces *Proc. IEEE VIS '02, Boston, USA* 163-170

[59] Lague D, Brodu N, Leroux J 2013 Accurate 3D comparison of complex topography with terrestrial laser scanner: Application to the Rangitikei canyon (N-Z) *ISPRS J. Photogramm. Remote Sens.* **82** 10-26

[60] Hoppe H, DeRose T, Duchamp T, McDonald J, Stuetzle W 1992 Surface reconstruction from unorganized points *Comput. Graph. (ACM)* **26** 71-78

[61] BS ISO 22514 part 7 2012 *Statistical methods in process management - Capability and performance - Part 7: Capability of measurement processes* (International Organization for Standardization)

[62] ISO 10360 part 4 2000 *Geometrical product specifications (GPS) - Acceptance and reverification tests for coordinate measuring machines (CMM) - Part 4: CMMs used in scanning measuring mode* (International Organization for Standardization)

[63] Leach R K, Carmignato S 2020 *Precision Metal Additive Manufacturing* (CRC Press)

[64] Eastwood J, Zhang H, Isa M A, Sims-Waterhouse D, Leach R K, Piano S 2020 Smart photogrammetry for three-dimensional shape measurement *Proc. SPIE* **11352** 115320A